

Unveiling the Degradation Mechanism of Sodium Ion Batteries Based on $\text{Na}_4\text{Fe}_3(\text{PO}_4)_2\text{P}_2\text{O}_7$ Cathode and Hard Carbon Anode Suggests Anode Particle Size Reduction for Cycling Stability

Shubham Lochab,^[a, b] Sagar Bharathraj,^[a] K. Subramanya Mayya,^[a] Prabeer Barpanda,^[b] and Shashishekhar P. Adiga^{*[a]}

To improve the cycle life of sodium-ion batteries, it is essential to understand the microscopic processes that lead to cell degradation. The mismatched response time of anode and cathode has profound but poorly understood impact on cycle life. In this work, we combine electrochemical and materials characterization along with electrochemical modeling to investigate the root cause of degradation in sodium-ion full cells made from $\text{Na}_4\text{Fe}_3(\text{PO}_4)_2\text{P}_2\text{O}_7$ (NFPP) cathodes and hard carbon (HC) anode. Our results pinpoint to the slow diffusion of Na in HC as the main cause of diffusional polarization that leads to

cathode experiencing high local potentials and ultimately to active material loss over cycling. We demonstrate that by reducing the anode particle size, the diffusional timescales in anode can be matched with that of cathode to improve both extractable capacity as well as cycle life. These observations shed light on non-intuitive and intricate ways in which cathode and anode can interact with each other to cause degradation in Na-ion batteries and how microscopic understanding of these cause and effects can help design long lasting batteries.

Introduction

The development of batteries made from earth-abundant materials is critical to secure a sustainable energy ecosystem. Notwithstanding the dominance of lithium-ion batteries (LIBs) in consumer electronics and electric mobility, the demand for critical minerals required to build LIBs is expected to outpace the supply. The mining and processing of scarce minerals used in LIBs such as Li, Co, Ni and Mn as well as graphite can lead to significant environmental and supply chain issues as well as high costs. In applications needing less stringent energy and power densities, such as stationary energy storage, e-scooters, e-taxis and delivery vehicles, alternate chemistries that use earth-abundant materials promise more sustainable and environmentally friendly batteries. While several different non-lithium chemistries involving monovalent (Na^+ , K^+) and multivalent ions (Zn^{+2} , Ca^{+2} , Al^{+3}) are being explored,^[1-7] Na-ion batteries (NIBs) have emerged as very promising candidates. This is primarily motivated by the fact that (i) sodium resources are more abundant, geographically uniformly distributed, and less expensive (ii) NIBs work on similar principles as LIBs since they belong to the same group in the periodic table and (iii)

many inexpensive host materials for Na on both anode and cathode sides have been identified.

Both oxides-based and polyanionic materials have been considered for cathode host materials.^[8] Polyanionic material are attractive since they provide tunable crystal structure that can be achieved by various synthesis methods, strong framework, and higher redox potential owing to the inductive effect. Further, crystals of polyanionic materials have a robust three-dimensional framework providing durability, required for long cycle life. From a synthetic point of view, mixed polyanionic systems, which have a combination of polyanionic species, offer the flexibility of using various synthesis method like solid state, sol-gel, solution combustion etc. One such mixed polyanionic is sodium iron pyrophosphate [$\text{Na}_4\text{Fe}_3(\text{PO}_4)_2\text{P}_2\text{O}_7$ or NFPP], belonging to the more general class of cathode materials with formulae $\text{Na}_4\text{M}_3(\text{PO}_4)_2\text{P}_2\text{O}_7$ ($\text{M}=\text{Mn, Fe, Co, Ni}$). NFPP with a theoretical capacity of 129 mAh g⁻¹ and an average discharge voltage of around 3.1 V, which is slightly higher in comparison to $\text{Na}_2\text{FeP}_2\text{O}_7$ (3.0 V), NaFePO_4 (2.7 V), NaFePO_4F (3.0 V) material,^[9-12] was first studied as a cathode material for sodium ion batteries in 2012 by Kim et al 2012.^[13] Its non-toxicity, stability under exposure to air, CO_2 and humidity and earth-abundant constituent materials make it very attractive. Further, the crystal structure of $\text{Na}_4\text{Fe}_3(\text{PO}_4)_2\text{P}_2\text{O}_7$ consisting of layers of $[\text{Fe}_3\text{P}_2\text{O}_{13}]^\infty$ and P_2O_7 groups linked by the pyrophosphate (P_2O_7) polyanionic groups, form tunnels which provide pathways for movement of Na^+ ion through a low activation barrier.

Most of the previous studies on NFPP focused on understanding and improving its properties as a cathode material in a half-cell configuration, specifically, utilizing carbon based functional materials to improve the electronic conductivity of the material. For example, NFPP/C carbon coated nanospheres with

[a] S. Lochab, S. Bharathraj, K. S. Mayya, S. P. Adiga
NextGen Projects, Samsung Advanced Institute of Technology, Samsung Semiconductor India Research, 560048 Bangalore India
E-mail: shashi.adiga@samsung.com

[b] S. Lochab, P. Barpanda
Faraday Materials Lab, Materials Research Centre, Indian Institute of Science, 560012 Bangalore India

Supporting information for this article is available on the WWW under <https://doi.org/10.1002/batt.202400025>

a template approach, delivering discharge capacity of close to the theoretical capacity of 129 mAh g⁻¹^[14] and NFPP/C nanocomposite using a sol-gel synthesis^[15–17] and have been reported. While later studies reported on full cells made with hard carbon, the cells showed significant degradation^[18] or needed the use of functional materials and specialized processing^[19] that may not translate to scalable synthesis. Practical approach to full cell fabrication by pairing with the inexpensive hard carbon anode and achieve long cycle stability are critical for stationary energy storage applications.

In this work, we demonstrate facile and scalable synthesis of NFPP cathode and hard carbon anode and full cell performance without the use of templates or functional carbon materials. First, we apply solution combustion to synthesize cathode, a simple process that consistently produces nanoparticles and is energy efficient. Ascorbic acid used as a precursor in the process forms a sp² carbon coating, which acts to enhance the electronic conductivity of the material, without the need for functional carbon materials. Secondly, and more importantly, we demonstrate by applying detailed electrochemical thermal modeling and ex situ materials characterization that the degradation seen in full cells with hard carbon is because of polarization caused by slow sodium diffusion in HC particles that in-turn restricts the state-of-charge (SOC) range experienced by the cathode to a narrow range of sodiation, resulting in reduction in extractable capacity. Further, because this also means the cathode experiences a high voltage where it is unstable, it begins to lose active material with cycling. We use this insight obtained by modelling and corroborated by battery cycling behavior and materials characterization to bring down the anode particle size to achieve improved extractable capacity and cycle stability, with more than 95% capacity retention after >200 cycles.

Results and Discussion

Materials Structure and Characterization of Active Electrode Materials

The synthesis of cathode active material employed the solution combustion method, involving a two-step procedure, resulting in the production of NFPP nanoscale particles with the added benefit of carbon coating. Rietveld refinement of XRD pattern (Figure 1a), obtained for the final NFPP combustion product, was done and corresponding structural images are shown in inset of the refinement. Rietveld refinement was conducted on the X-ray diffraction pattern of the combustion product, Na₄Fe₃(PO₄)₂P₂O₇, yielding structural parameters and atomic coordinates as provided in Table S1. A trace amount (5.2%) of electrochemically inactive NaFePO₄ impurity was found. The material has an orthorhombic structure with Pn2₁a symmetry, featuring mixed phosphates, phosphate tetrahedra (PO₄), pyrophosphate [P₂O₇ (PO₄-PO₄)] groups, and iron (+2) (FeO₆) octahedral, as previously reported by other works. Electron microscopy techniques (SEM and TEM) were employed to assess the material's morphology. Spherical particles in the range of

50–150 nm were observed in SEM images (Figure 1 c-d), forming agglomerates due to dehydration reactions during phosphate group condensation/polymerization. TEM studies revealed highly crystalline nanoparticles with HRTEM and SAED patterns confirming the polycrystalline nature of the material (Figure 1e-g). Elemental mapping for the material (Figure 1h) showed a homogeneous distribution of the elements present. Cross-sectional SEM images of cathode coatings used for electrochemical analysis were captured to verify coating thickness (Figures S1). Vibrational spectroscopy, including FT-IR and Raman spectroscopy, was employed to investigate the material's local structure. The FT-IR spectrum (Figure S2a) exhibited intramolecular vibrations originating from phosphate (PO₄) tetrahedra, while Raman spectroscopy (Figure S2b) revealed the presence of a carbon coating based on the D and G bands. An I_D/I_G intensity ratio of 0.95 indicated a high degree of crystallinity. XPS was conducted to confirm the elemental composition and purity of the mixed phosphate Na₄Fe₃(PO₄)₂P₂O₇ material. The spectra (Figure S3) verified the presence of Na, Fe, O, and P elements in the sample, with Fe confirmed to be in the +2 oxidation state.

The material's electrochemical properties were evaluated by using it as a cathode material in sodium-ion half-cell testing. Galvanostatic cycling within the potential range of 1.8–3.8 V using 1 M NaPF₆ in EC:DEC revealed reversible voltage profiles with multiple plateau regions (Figure 1b), each corresponding to different sodium (Na⁺) intercalation sites. The durability of the structure during cycling was attributed to a fourth Na site. A discharge capacity of 121.1 mAh g⁻¹ was observed from the second cycle onwards, indicating approximately 2.8 sodium ions (de)intercalation per formula unit. The cyclic voltammograms (Figure S4b) displayed Fe redox behaviour, with an average potential of 3.1 V. Rate capability studies of NFPP (Figure S4c, d) exhibited a good discharge capacity even at a high rate of 2C, highlighting its potential as a sodium-ion battery material.

The anode active material HC was synthesized using pyrolysis of sucrose. Cross-sectional SEM image (Figure S5) of the anode coating on the current collector allowed us to measure the active material thickness and verify the coating quality. SEM images of as prepared HC showed that the particle size varied from 4 to 8 μm (Figure S6). Raman analysis to analyze the local structure resulted in a spectrum (Figure S7) consisting of characteristic D (~1350 cm⁻¹) and G (~1579 cm⁻¹) bands. An I_D/I_G intensity ratio of 0.97 implied presence of predominantly sp² carbon.

Electrochemical Performance and Characterization of NFPP/HC Full Cells

To assess the electrochemical performance of Na₄Fe₃(PO₄)₂P₂O₇ for practical applications, a full cell configuration was employed, with Na₄Fe₃(PO₄)₂P₂O₇ serving as the cathode and hard carbon as the anode material. Prior to establishing the full cell, electrochemical cycling of the hard carbon anode was conducted in a half-cell setup against sodium (Na) for five cycles to

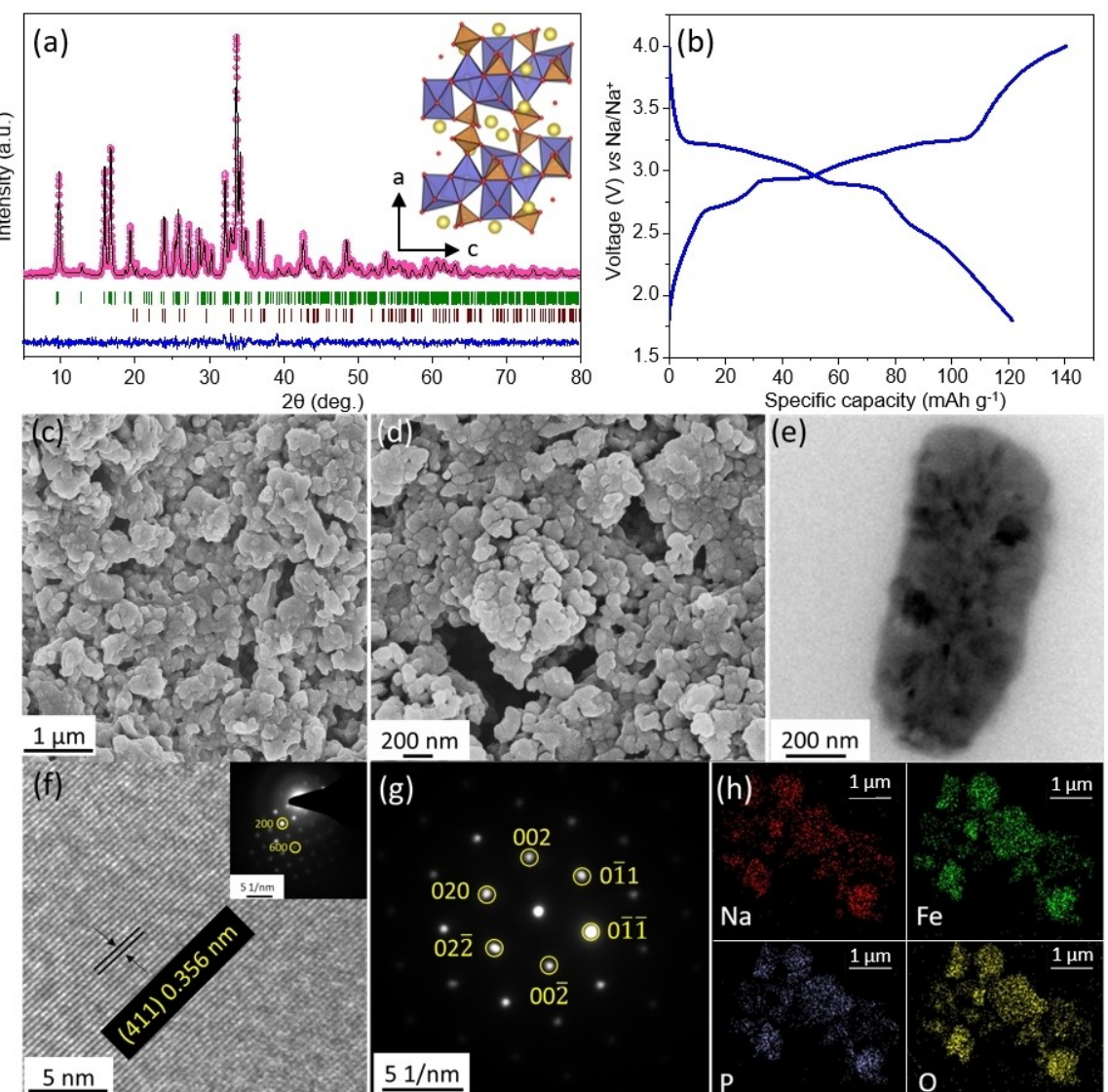


Figure 1. (a) Rietveld Refinement shown for the powder XRD pattern of $\text{Na}_4\text{Fe}_3(\text{PO}_4)_2\text{P}_2\text{O}_7$ having space group $Pn2_1a$. The observed data points in pink, calculated pattern in black, difference in dark blue and Bragg positions in green color, Bragg positions for NaFePO_4 in wine color. Inset shows the crystal structure projection with the FeO_6 polyhedra in purple, $\text{PO}_4/\text{P}_2\text{O}_7$ tetrahedra in orange, sodium atoms in yellow color. (b) Galvanostatic (dis)charge curve for $\text{Na}_4\text{Fe}_3(\text{PO}_4)_2\text{P}_2\text{O}_7$ material at rate of C/20. Morphology of $\text{Na}_4\text{Fe}_3(\text{PO}_4)_2\text{P}_2\text{O}_7$ material (c, d) Scanning electron microscopy (SEM), (e) Transmission electron microscopy (TEM) image (f) HRTEM image showing the interlayer spacing. Inset of f and (g) SAED pattern showing various spots confirming the crystalline nature of the material. (f) Elemental mapping with a homogeneous distribution of Na (red), Fe (green), P (violet), O (yellow).

establish a stable solid electrolyte interface (SEI) film. The mass ratio for the cathode and anode was maintained to be 2.1:1, to maintain the capacity match between NFPP cathode and HC anode. The corresponding (dis)charge profiles for the anode are presented in Figure S8. As depicted in the figure, the coulombic efficiency of the anode gradually stabilizes over time.

Figure 2a illustrates the galvanostatic (dis)charge curves for the $\text{Na}_4\text{Fe}_3(\text{PO}_4)_2\text{P}_2\text{O}_7$ /hard carbon full cell within a voltage window of 0.7–3.2 V, operated at a current rate of C/25. In Figure 2b specific capacity value determined based on the mass of the active cathode material is plotted as a function of cycling. It is noteworthy that in the initial cycles, the full cell exhibits a specific capacity reaching up to 100 mAh/g. However, a 50% reduction in specific capacity within 65 cycles seen subse-

quently, which is a significant degradation. Such severe degradation has been reported earlier for NFPP full cells with HC anode,^[18,19] however, the source of the degradation, specifically why pairing NFPP with HC in a full cell leads to accelerated degradation has not been investigated.

Source of Cell Degradation

To investigate the mechanism of cell degradation, we initiated our analysis by examining the charge-discharge cycling profiles to discern whether degradation stemmed from an increase in cell internal resistance or active material loss. Both the IR drop and EIS data (Figure S9) revealed that cell internal resistance

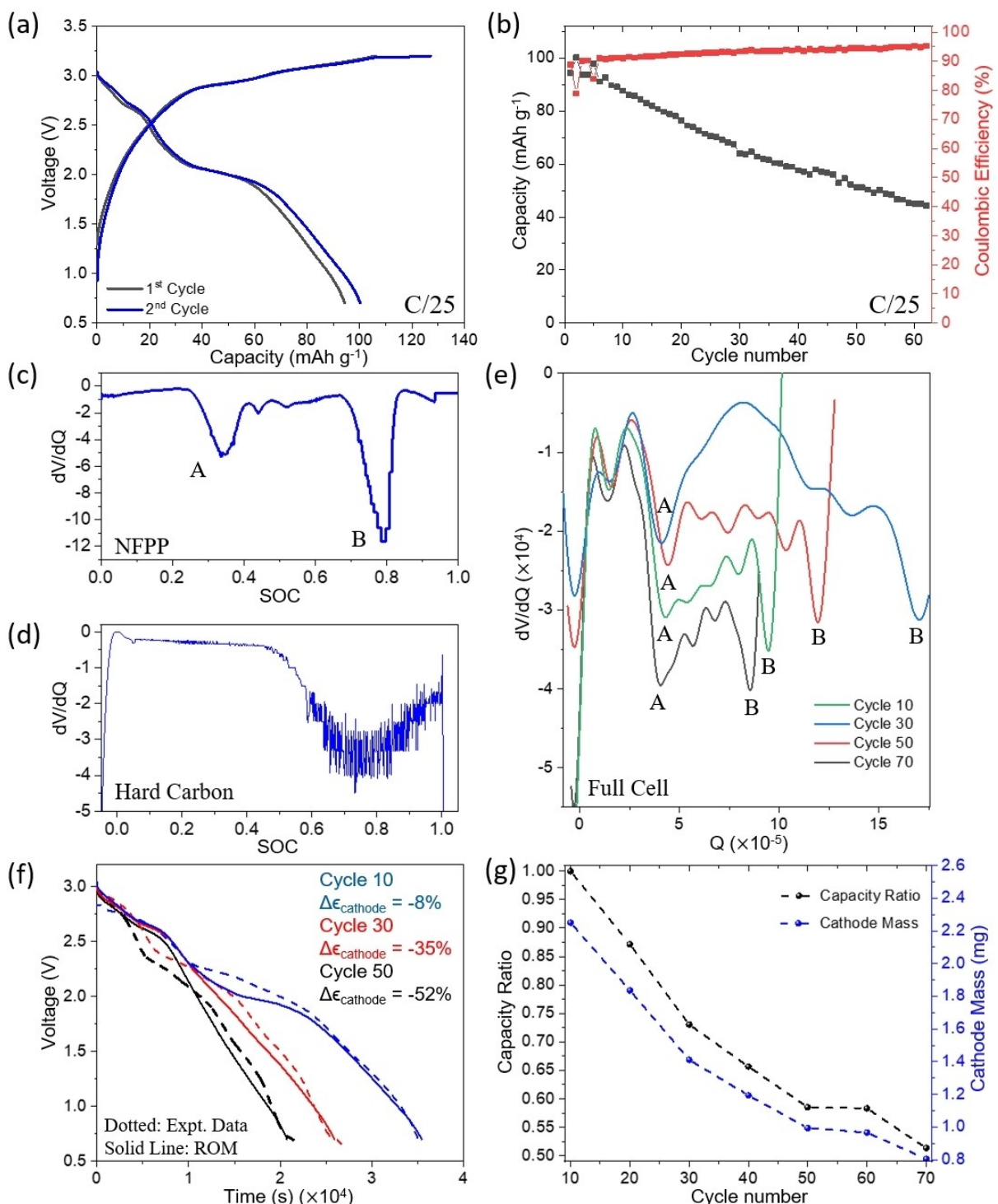


Figure 2. (a) Galvanostatic (dis)charge curves of NFPP/HC full cell cycled between voltage range of 0.7–3.2 V cycled at C/25. (b) Change in specific capacity with increasing number of cycles. Incremental capacity analysis for quantification of degradation: The dV/dQ Vs SOC curves for both the Cathode (NFPP) and Anode (Hard Carbon) half cells are shown with a fit in (c) & (d) respectively. The dV/dQ Vs the capacity, Q , for the full cell is shown in (e). (f) Discharge profiles for different cycle numbers for the NFPP/HC full cell cycled between voltage range of 0.7–3.2 V at C/10. The ROM profiles (dashed lines) are overlaid on top of the experimental data, whereby the cathode volume fraction has been reduced to match the discharge capacity for the particular cycle number. (g) Variation of the full-cell discharge capacity and cathode mass, as derived from ICA, as a function of the cycle number, for the NFPP/HC full cell cycled between voltage range of 0.7–3.2 V at C/10.

and charge transfer resistance increased marginally with cycling, however, not enough to cause severe degradation seen in the cell performance. Subsequently, we conducted incremen-

tal capacity analysis (ICA) by plotting dV/dQ against discharge capacity as the cell discharged. The identification of distinctive features corresponding to the cathode and anode in full cell

data, based on cathode and anode half-cell dV/dQ curves (Figures 2c and 2d, respectively), is detailed in the SI. In the case of NFPP half cell, NFPP exhibited two prominent dips, labeled as A and B, in the dV/dQ plotted against state of charge (SOC), as illustrated in the half-cell data in Figure 2c. Since these two features occur at the same SOC values irrespective of the active material content, the distance between them when multiplied by integral current passed between those two points normalized by the specific capacity of the material between those two points gives the active material mass. In the full cell dV/dQ plot shown in Figure 2e, the distance between features A and B progressively decreased as cycling progressed, indicating a reduction in cathode active material. We quantified this decrease in cathode active material as a function of the number of cycles by scaling the original active material content using a factor corresponding to the distance between these features. This quantification is presented in Figure 2g alongside cell capacity, revealing a direct correlation between cell capacity decrease and active material loss. To further validate that cathode active material is indeed the source of degradation, we conducted ROM simulations to demonstrate the impact of degradation on cell discharge behavior, considering the extracted cathode active material content for a given cycle number. The details of ROM simulations are given in the methods section and the parameters used in ROM simulations are given in Table S3. In Figure 2f, we compared discharge curves from ROM simulations with experimental discharge curves for different cycle numbers. The remarkable agreement between simulated and experimental data lends strong support to the conclusion that degradation primarily results from cathode active material loss.

The source of capacity fade becomes even more apparent through the comparison of *ex-situ* material characterization before and after cycling. The cycled cathode was cleaned with EC and DEC solvents, which are the solvents present in the electrolyte (1 M NaPF₆ in EC:DEC), before carrying out the *ex situ* studies. Ex situ analysis was done for the pristine (before cycling) and cycled NFPP/HC full cell shown in Figure 2a-b, cycled for 63 cycles at C/25 rate using Raman spectroscopy, scanning electron microscopy (SEM), transmission electron microscopy (TEM), and X-ray photoelectron spectroscopy (XPS) characterization techniques. The increase in D band to G band ratio (I_D/I_G) from 0.96 for the pristine cathode to 1.05 for the cycled cathode in Raman spectroscopy (Figure S10) revealed that the graphitic carbon coating present underwent some structural disorder and fraction of sp^2 carbon increased marginally. The phosphate (PO₄) and pyrophosphate (P₂O₇) stretching and bending vibrations are visible in the wavenumber region 400 cm⁻¹ to 1200 cm⁻¹, while they appear to decay in the intensity for cycled cathodes, actual intensity is similar for pristine and cycled cathodes. A similar increase in the I_D/I_G ratio from 0.98 to 1.08 is observed for the HC anode as well, as shown in Figure S11, indicating some disorder post cycling. However, since there is no split in D and G bands a complete structural disorder is not implied.

SEM images for pristine NFPP cathode show particles of micrometer scale (2–5 μm) with definite features. EDS mapping

confirmed the presence of Na, Fe, P, O elements with uniform distribution as well. Figure S12 shows the SEM Image of a fresh NFPP cathode (front view) along with the energy dispersive spectroscopy (EDS) elemental mapping. Interestingly, *ex situ* SEM images of the cycled cathode (Figure 3a-d), revealed the presence of spherical shaped deposits of around 20 μm distributed on the coating. This hints at possible degradation happening on the cathode side in the full cell configuration. From the EDS mapping of the cycled cathode (Figure 3e-i), it was observed that only Na and O elements were present in the spherical deposits obtained on the cathode coating. This suggested a possible degradation of the cathode to form a species containing only Na and O atoms. SEM images of pristine and cycled hard carbon anode are shown in Figure S13(a)–(d) show the pristine hard carbon with particle size of around 2 μm with definite shape and features, on the copper foil. After cycling in the full cell configuration, the cycled anode particles could be seen to lose their definitive shape, which was present before cycling.

HRTEM images of Na₄Fe₃(PO₄)₂P₂O₇ cathode for both pristine and cycled materials are shown in Figure S14. The cathode was recuperated post cycling of the full cell and subjected to TEM operation. The HRTEM images confirm the crystallinity of Na₄Fe₃(PO₄)₂P₂O₇ cathode, with distinct planes (212) and (302) visible for the pristine and cycled cathode, respectively. This observation suggests that the crystalline structure of NFPP cathode remains intact post cycling as well. However, it is worth noting that TEM is a highly focused technique, and it may not represent the crystallinity of all regions within the NFPP cathode post cycling. The characterization of the spherical deposits (Figure 3), couldn't be achieved through HRTEM due to its limitations.

Figure S16 shows change in XPS spectra for Fe and Na elements for pristine and cycled cathode in the full cell configuration. There is an increase in the intensity of Na 1s peak at 1071.8 eV post cycling which is clearly visible from the spectra. Since, we know XPS is a surface sensitive technique, the increase in the Na element intensity can be correlated with the micrometric spherical deposits containing Na, observed in EDS mapping of the cycled cathode in full cell configuration as well (Figure 3a-d). While analyzing the Fe 2p spectra, a split can be seen which is due to spin-orbital coupling. For the pristine cathode, binding energy of Fe 2p_{1/2} and Fe 2p_{3/2} were found to be 724 eV and 711 eV which corresponds to the +2 oxidation state of the Fe atom. Same values of binding energy for Fe 2p_{1/2} and Fe 2p_{3/2} for cycled cathode were obtained as well, indicating +2 oxidation state. Though there was a change in the intensity of the 2p_{3/2} satellite peak post-cycling, which implies the presence of a mixed oxidation state of Fe, i.e., Fe⁺² and Fe⁺³. In pristine cathode, there is presence of two strong satellite peaks at and binding energy. Since, the satellite peak primarily depends on the local environment of the Fe atom, this kind of change post-cycling hints at some change which may be due to Na and O atoms leached out of the lattice. This information in combination with the SEM EDS mapping for the cathode hints at major changes happening on the NFPP leading to a decay in the specific capacity of the NFPP/HC full cell

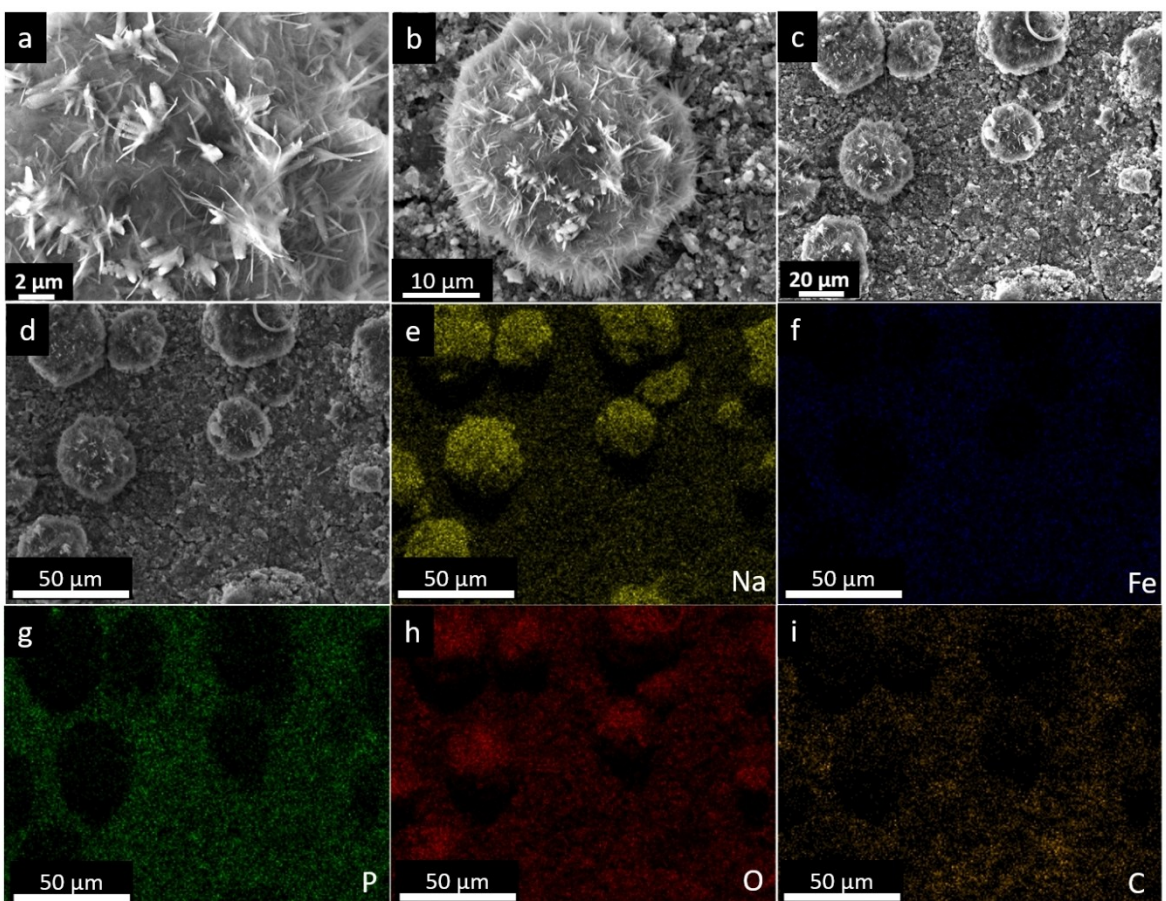


Figure 3. SEM Images of: (a)-(d) cycled cathode $\text{Na}_4\text{Fe}_3(\text{PO}_4)_2\text{P}_2\text{O}_7$ material, (e)-(i) Energy dispersive spectroscopy (EDS) mapping for various elements present in the cathode. Formation of spherical deposits on the surface of the cathode material is visible.

through loss of sodium from the NFPP lattice. Fe atom could also be present in mixed oxidation state post cycling which would imply the (de)insertion is not happening completely for the NFPP/HC full cell. Though it should be noted that XPS is a majorly a surface technique and predicting the bulk properties or mechanism is tough using this technique.

Keeping this in mind, considering the size of the cathode coating, which is approximately 7 μm as shown in Figure S1, we conducted depth sputtering analysis at two distinct depths: 200 nm and 2000 nm. The corresponding outcomes are presented in ESI Figure S21. Notably, both depths exhibited an additional peak in the $\text{Fe } 2p_{3/2}$ region. This finding suggests the presence of mixed oxidation states of Fe within the bulk material. These results align with our previous findings, indicating that mixed oxidation states of Fe persist even after cycling, indicating incomplete (de)insertion within the cathode due to material decomposition.

Moreover, a comparative analysis of the Na XPS sputtering data at 200 nm and 2000 nm revealed no significant increase in intensity, unlike the surface XPS results depicted in Figure S21. This inconsistency implies that the rise in Na content primarily occurs at the surface, likely due to the formation of micrometric spherical deposits.

To gain a deeper understanding of degradation, we analyzed full cell cycling behavior at various charge voltage cut-offs. Figure 4a illustrates capacity degradation over cycles at charge cut-off voltages of 3.2, 3.4, and 3.6 V with a C/5 current. While higher cut-offs lead to increased capacity, they also elevate the degradation rate. This prompted a closer examination of charge-discharge curves, particularly focusing on solid-state diffusion-related polarization due to the low diffusivity of Na atoms in HC (refer to Figure 5 for diffusivity vs SOC of cathode and anode). In Figure 4b, the discharge behavior at C/5, followed by a rest period, reveals a slow voltage recovery of close to 1 V, indicating diffusional polarization. This behavior, stems from the fact that slow solid state diffusion causes concentration gradients inside anode particles and the equilibration during rest period leads to uniform Na distribution inside the particles which in turn is reflected by the cell's open circuit voltage recovery, a function of particle surface concentration. This effect, also confirmed by ROM simulation, forces the system to operate sub-optimally, reducing extractable capacity. Moreover, Figures 4c and 4d show extreme SOC and electrode potentials, especially for the cathode, resulting in low SOC (0.06) and high OCP (> 3.8 V) experienced due to the high polarization. These conditions may render NFPP crystals unstable, causing the loss of cathode active material as some

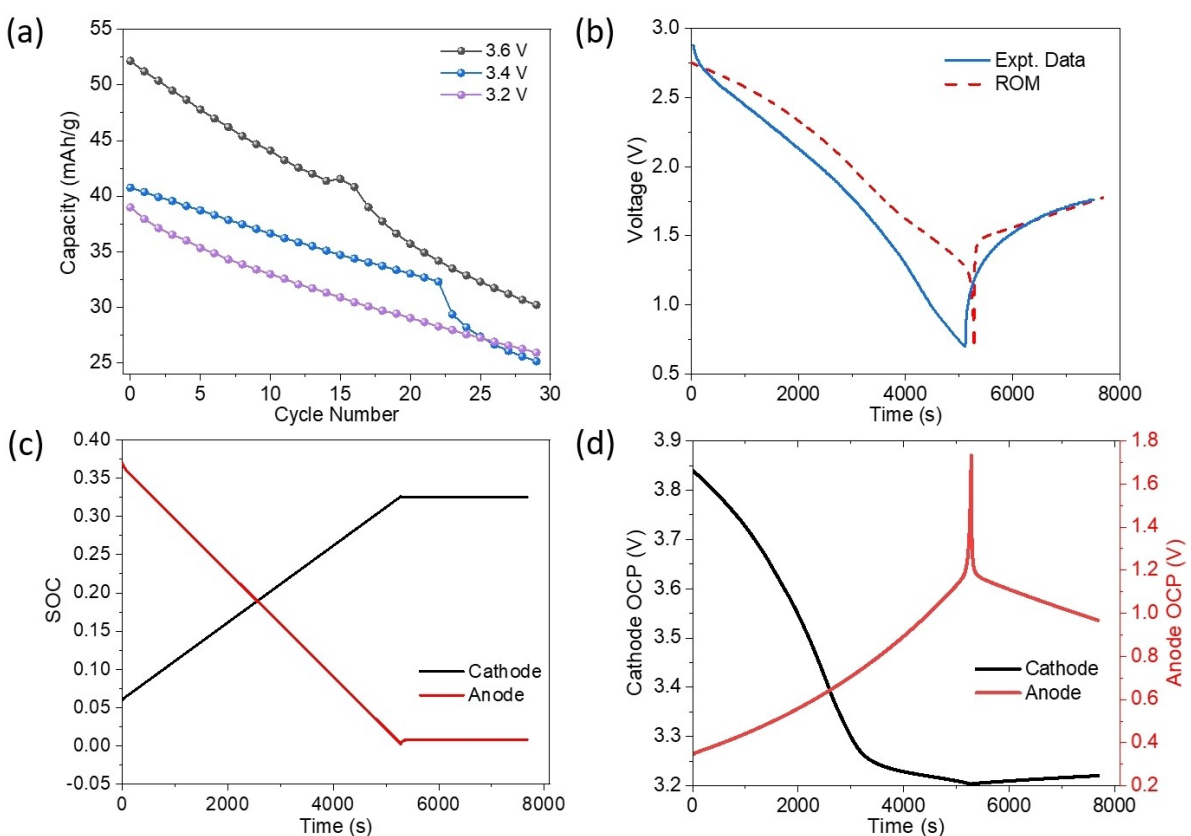


Figure 4. Degradation analysis: (a) Capacity reduction as a function of cycling for different charge cut-off voltages at a C/5 cycling current. (b) Comparison of ROM simulated and experimental discharge profile at C/5, including the rest period that shows voltage relaxation post discharge. (c) SOCs experience by cathode and anode during discharge. (d) The OCPs experience by cathode and anode during discharge.

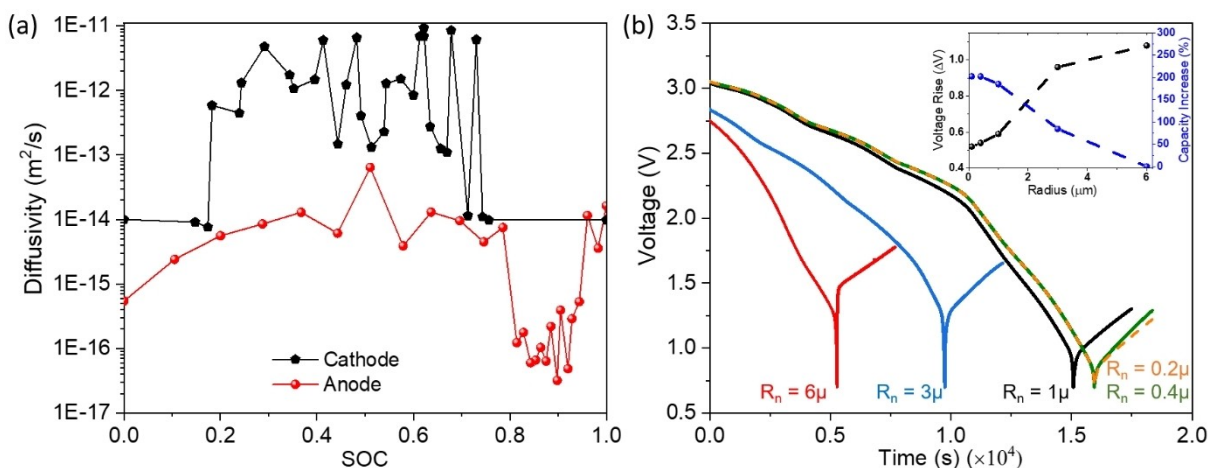


Figure 5. (a) Variation of diffusion coefficients of cathode and anode as a function of electrode SOC as determined from GITT. (b) Comparison of ROM discharge curves for at C/5 for different anode radii, showing the post discharge recovery as well. The inset plot shows the total voltage rise post discharge and extractable capacity change with the anode radius.

unit cells may lose the fourth Na, corroborated by EDS mappings of the particle deposits as shown by ex situ analysis of the cathode. In conclusion, high anode diffusional polarization not only diminishes extractable cell capacity but also induces cathode material loss through exposure to unstable potentials.

Achieving Cycle Stability by Reducing Anode Particle Size

Back-of-the-envelope calculations suggested that the characteristic diffusion time (R^2/D) in 4 μm particles is 3×10^5 s vs 2×10^3 s in 1 μm particles. Based on the insights from analyses above, we pursued anode particle size reduction as a strategy to reduce diffusional polarization and to see if it improved the

extractable capacity and reduced cell degradation. As prepared HC was spex milled to reduce the average particle size from 6 μm to 0.4 μm . The galvanostatic discharge curves at C/5 current for half cell HC are compared for before and after milling are compared in Figure S15a & b, where the post charge voltage relaxation drops by ~ 0.75 V post milling indicating a reduction in diffusional polarization. The SEM images shown in Figure S15c & d show a clear decrease in particle size post milling. The positive impact of reducing the HC particle size on rate capability on HC half-cell is clearly evident in Figure S20 where extractable capacity and Coulombic efficiency are plotted for different discharge rates. The cell capacity for the half cell with milled HC was higher for all C-rates tested. The reduction in the anode size and thus the diffusional polarization, helps in recovering the extractable capacity, especially at higher C-rates in full-cell as well, as shown in Figure 6. For example, the C/5 capacity increased from 42 mAh g^{-1} before milling to 85 mAh g^{-1} after milling. The capacity reduced to 74 mAh g^{-1} at C/2, which is significant considering that the full cell was unable to cycle at C/2 before milling. Further, the columbic efficiency improves post milling/reduction of the anode size for all C-rates. Most importantly, the cell capacity saw very little degradation post milling even after more than 200 cycles. Thus, our hypothesis that large diffusional polarization in the HC anode causes reduced cell capacity and pushes the cathode to SOC windows of operation where NFPP is unstable is further substantiated with this result.

Conclusions

In conclusion, this research work demonstrates an advancement in sodium-ion battery technology through the successful fabrication of highly cycle-stable full cells made out of NFPP and hard carbon. These cells exhibited a specific capacity of 80 mAh g^{-1} at C/2 current and retained the capacity after

several hundred cycles. The use of earth-abundant materials and facile fabrication methods for both cathode and anode further underscore its promising practical applicability. The path to achieving cycle-stability included identification of cathode active material loss as the primary mechanism of degradation and that the slow anode Na-diffusion related polarization led to reduced capacity and increased cathode degradation. Further, the use of detailed electrochemical models allowed us to conclude that reducing the particle size of as prepared anode particles would help reduce the polarization and hence diffusion related overvoltage. By bringing the anode particle size down to 0.4 μm , the overvoltage was reduced that resulted in increase in extractable capacity as well as cycle life. This work serves as a significant milestone toward achieving inexpensive, sustainable energy storage technology, specifically for stationary storage.

Materials and Methods

Synthesis of $\text{Na}_4\text{Fe}_3(\text{PO}_4)_2\text{P}_2\text{O}_7$ Cathode Material

Solution combustion synthesis (SCS) method was used to synthesize the mixed phosphate based material. Ferric nitrate ($\text{Fe}(\text{NO}_3)_3$), Sodium dihydrogen phosphate (NaH_2PO_4), and ascorbic acid ($\text{C}_6\text{H}_8\text{O}_6$) precursors were taken in stoichiometric amounts according to target material. Ascorbic acid acts as the fuel as well as the reducing agent to convert the Fe^{+3} to Fe^{+2} ion in the solution. Approximately, 50 mL distilled water was used for dissolving the precursors. Further stirring was done at 120 °C till complete evaporation of water. Further temperature was raised till 300 °C using a hot plate. Ascorbic acid led to the exothermic combustion of the precursors leading to the intermediate product. Annealing of the intermediate was done at 600 °C for 12 h with Ar flow maintained throughout to get final *in-situ* carbon coated product.

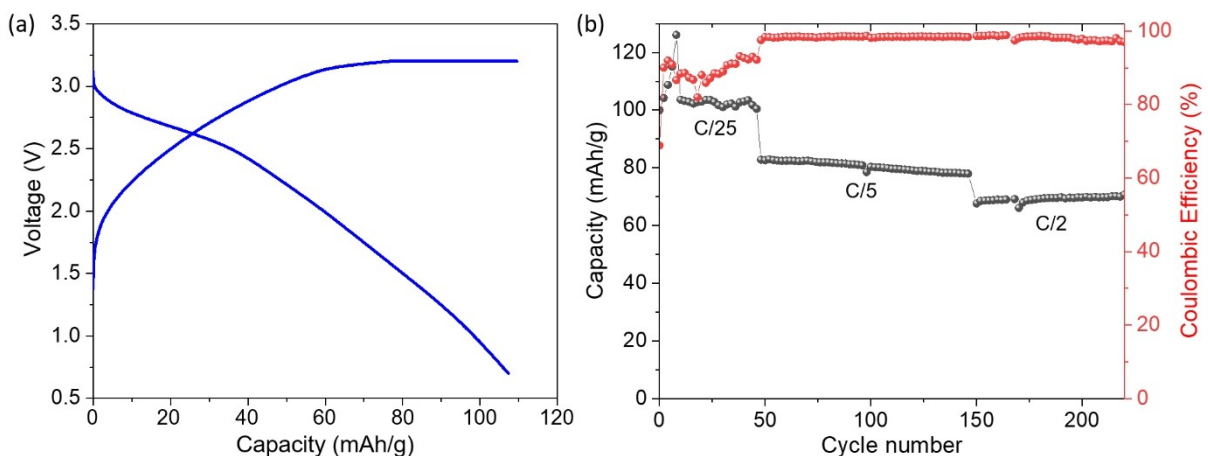


Figure 6. (a) Galvanostatic (dis)charge curves of NFPP/HC full cell cycled between voltage range of 0.7–3.2 V at C/25 post spex milling treatment of the HC anode for 45 mins. (b) Change in specific capacity and coulombic efficiency with increasing number of cycles.

Synthesis of Hard Carbon Anode Material

Hard carbon was synthesis using pyrolysis of sucrose. First dewatering of the sucrose was done at a lower temperature followed by carbonization at higher temperature. 1 M sucrose solution was heated in an autoclave via a hydrothermal process at 190 °C for 12 hours to obtain a black coloured powder. The obtained product was carbonised at a temperature of 1100 °C in Ar atmosphere in a tubular furnace.

Material Characterization

XRD Powder X-ray diffraction patterns were collected for the $\text{Na}_4\text{Fe}_3(\text{PO}_4)_2\text{P}_2\text{O}_7$ material using PANalytical X'Pert Pro diffractometer having a Cu-K α radiation source ($\lambda = 1.5404 \text{ \AA}$) at 40 kV and 30 mA. A 2 θ range of 5–80° was selected for data acquisition (scanning step: 0.026°), in Bragg-Brentano geometry. Rietveld refinement was done for the XRD data to get the crystal structure parameters using FullProf Suite. VESTA software was used to exhibit crystal structure of the material. The morphology of the material was seen using a FE-SEM, FEI Inspect F 50 operated at 10 kV, equipped with an energy-dispersive X-ray analysis (EDS) instrument for quantification of elements. HRTEM (High-resolution TEM) and SAED (Selected Area Electron Diffraction) patterns were also collected using an FEI Tecnai T20 U-Twin TEM microscope operated at 200 kV. X-ray Photoelectron Spectroscopy was done using a Kratos Axis Ultra DLD with an Al K α X-ray at 13 kV. For the collected XPS data, shift corrections were done in accordance with binding energy of carbon as the reference at 284.6 eV. Depth sputtering XPS measurements were carried out for the cycled cathode at 200 nm and 2000 nm depth. LabRAM HR (Horiba Jobin Yvon) instrument with 532 nm laser source (green) was used to collect Raman spectra at a spectral resolution of 1 cm $^{-1}$ and spatial resolution of 2.5 nm. FT-IR spectra was collected using Perkin Elmer (Frontier) instrument with KBr diluted powder.

Electrochemical Measurements

For the electrochemical measurements for the material, a working electrode was prepared according to an 8:1:1 mass ratio of active material [$\text{Na}_4\text{Fe}_3(\text{PO}_4)_2\text{P}_2\text{O}_7$], Super-P conducting Carbon black and polyvinylidene fluoride (PVDF) binder respectively. These were mixed properly using adequate N-Methyl-2-pyrrolidone (NMP) leading to formation of a thick slurry. The slurry obtained was further coated on aluminium (Al) foil with further drying in vacuum. The active material loading for each coating was approximately 2–4 mg cm 2 . The material electrochemical properties were seen for Na half-cell using 1 M NaPF_6 /EC:DEC (Kishida Chem., battery grade) as electrolyte. Sodium metal foil was used as the counter electrode in the half cell. Galvanostatic intermittent titration technique (GITT) as well as Potentiostatic intermittent titration technique (PITT) measurements were done using Bio-Logic BCS-805/810 to analyse the underlying (de)intercalation mechanism along with the chemical diffusion

coefficient. Hard carbon anode material was also tested for Na-ion batteries following the similar procedure as mentioned above, with hard carbon used as the active material. Full cells measurements were done for $\text{Na}_4\text{Fe}_3(\text{PO}_4)_2\text{P}_2\text{O}_7/\text{HC}1100$ using CR2032 coin cells. The slurry for the cathode and anode were coated on aluminium and copper current collectors, respectively. Same electrolyte as well as separator were used as those in the half-cell configuration. Full cell cycling was done in a voltage range of 0.7–3.2 V.

Bond Valence Site Energy Calculations

With the help of Bond valence site energy (BVSE) method, Na-ion energy barrier and the diffusion pathways were found for the $\text{Na}_4\text{Fe}_3(\text{PO}_4)_2\text{P}_2\text{O}_7$ material. This method analyses the vacancies as well as the variable coordination number of the sodium ions in the given local structure. The input required is the information files obtained from ICSD and Rietveld refinement after complete geometric optimization. Pathways for Na-ions diffusion are found in accordance with low bond valence site (E_{BVSE}). For the movement of sodium ions between two nearby sites, the low bond valency sites can be connected to visualize the pathway. In a report by Adam et al, softBV interface for calculation of the energy barrier present with the help of the bond valence mismatch $|\Delta V|_{\text{Na}-x} = \exp [-(R_{0,\text{Na}-x} - R_{\text{Na}-x})/b_{\text{Na}-x}]$ was reported. The bond valence mismatch can be seen in terms of an absolute energy scale by expressing the value of bond valence site energy of sodium (Na^+) cation surrounded and coordinated by X $^-$ anions. For local structures, migration pathways can be mapped out using this method and algorithm.

Electrochemical Modeling

To model the electrochemical behaviour of the full cells we applied a physics-based reduced order electrochemical model (ROM). ROM captures the nuances of the battery system, with a significantly better computational efficiency, as compared to pseudo 2-dimensional (P2D) based modelling. These electrochemical-thermal (ECT) models of batteries have been widely used and successful in understanding, predicting and optimizing battery states, performance.^[20] The P2D model of LIBs was conceptualized by John Newman's group.^[21] The mathematical network consists of partial/ordinary differential equations (PDE/ODEs), which absorbs battery physics by representing their electrochemical behaviour in terms of first principles based on mass, charge, energy conservation equations. With appropriate initial, boundary conditions through fluxes and state continuity equations, accurate and detailed profiles of important battery states and variables was made possible. However, when it came to practical implementation and ease of analysis, the bulky equations and heavy computations are an impediment. Reduced Order Models (ROM) as appropriately named, provides an alternative, computationally friendly environment, as compared to the P2D-ECT model without compromising on the efficacy and detailing. In ROM, the P2D network of PDEs and ODEs are

compressed to a set of ODEs and algebraic expressions respectively, to form a system of differential algebraic equations or DAEs.^[22] The compression in the spatial dimension happens through a process of volume averaging, where the spatial dimension is subject to domain averaging and the spatial information is later retrieved by appropriate profile approximations. Unlike the full order ECT, where numerical solvers are engaged to get converging solutions, ROM can be easily solved by explicit time-marching schemes leading to a numerically stable, grid independent, computationally friendly, robust and accurate state estimations. The isothermal version of ROM,^[22] was given an additional boost, in the form of a lumped thermal module, which accurately predicts the battery temperature spanning different and extreme operating conditions. A lumped form of the detailed thermal balance equations^[23] was introduced, accounting for all the sources and sinks of heat, without compromising on the accuracy leading to a Reduced Order Thermal Model or ROTM.^[24] The ROTM framework, its equations, validation with actual experimental data and other details are available in our previous works^[24] and readers are requested to refer to the same for more details. The same ROTM has been used in this study to model the Na-Ion system as both Li-Ion and Na-Ion essentially work on the principle of intercalation. The parameters used in the model are provided in Table S3. The Na diffusivity in cathode and anode are derived from Galvanostatic Intermittent Titration Technique (GITT). The kinetic studies involving GITT to measure diffusivity and the estimated diffusivity of Na in NFPP and HC are provided in Figures S18, S19, Figure 5.

Acknowledgements

The current work was financially supported by the Technology Mission Division (DST, Government of India) under the Materials for Energy Storage (MES-2018) program (DST/TMD/MES/2k18/00217). S.L. is grateful to the Ministry of Human Resource Development (MHRD, Government of India) for financial assistance. P.B. is grateful to the Alexander von Humboldt Foundation (Bonn, Germany) for a 2022 Humboldt fellowship for experienced researchers. Samsung authors acknowledge financial support from SAIT-Korea for this work.

Conflict of Interests

The authors declare no conflict of interest.

Data Availability Statement

The data that support the findings of this study are available from the corresponding author upon reasonable request.

- [1] N. Yabuuchi, K. Kubota, M. Dahbi, S. Komaba, *Chem. Rev.* **2014**, *114*, 11636–11682.
- [2] J.-Y. Hwang, S.-T. Myung, Y.-K. Sun, *Chem. Soc. Rev.* **2017**, *46*, 3529–3614.
- [3] M. H. Han, E. Gonzalo, G. Singh, T. Rojo, *Energy Environ. Sci.* **2015**, *8*, 81–102.
- [4] P. Barpanda, L. Lander, S. Nishimura, A. Yamada, *Adv. Energy Mater.* **2018**, *8*, 1703055.
- [5] M. Dahbi, N. Yabuuchi, K. Kubota, K. Tokiwa, S. Komaba, *Phys. Chem. Chem. Phys.* **2014**, *16*, 15007–15028.
- [6] K. Kubota, S. Komaba, *J. Electrochem. Soc.* **2015**, *162*, A2538–A2550.
- [7] R. Rajagopalan, Y. Tang, X. Ji, C. Jia, H. Wang, *Adv. Funct. Mater.* **2020**, *30*, 1909486–1909521.
- [8] P. Barpanda, *Chem. Mater.* **2016**, *28*, 1006–1011.
- [9] H. Kim, I. Park, S. Lee, H. Kim, K.-Y. Park, Y.-U. Park, H. Kim, J. Kim, H.-D. Lim, W.-S. Yoon, K. Kang, *Chem. Mater.* **2013**, *25*, 3614–3622.
- [10] J. Yan, X. Liu, B. Li, *Electrochim. Commun.* **2015**, *56*, 46–50.
- [11] C.-Y. Chen, K. Matsumoto, T. Nohira, C. Ding, T. Yamamoto, R. Hagiwara, *Electrochim. Acta* **2014**, *133*, 583–588.
- [12] W. Tang, X. Song, Y. Du, C. Peng, M. Lin, S. Xi, B. Tian, J. O. Zheng, Y. Wu, F. Pan, *J. Mater. Chem. A* **2016**, *4*, 4882–4892.
- [13] H. Kim, I. Park, D.-H. Seo, S. Lee, S.-W. Kim, W. J. Kwon, Y.-U. Park, C. S. Kim, S. Jeon, K. Kang, *J. Am. Chem. Soc.* **2012**, *134*, 10369–10372.
- [14] X. Pu, H. Wang, T. Yuan, S. Cao, S. Liu, L. Xu, H. Yang, X. Ai, Z. Chen, Y. Cao, *Energy Storage Mater.* **2019**, *22*, 330–336.
- [15] X. Wu, G. Zhong, Y. Yang, *J. Power Sources* **2016**, *327*, 666–674.
- [16] X. Ma, X. Wu, P. Shen, *ACS Appl. Energ. Mater.* **2018**, *1*, 6268–6278.
- [17] X. Ma, Z. Pan, X. Wu, P. K. Shen, *J. Chem. Eng.* **2019**, *365*, 132–141.
- [18] M. Chen, W. Hua, J. Xiao, D. Cortie, W. Chen, E. Wang, Z. Hu, Q. Gu, X. Wang, S. Indris, S. Chou, S. Dou, *Nat. Commun.* **2019**, *10*, 1480.
- [19] Y. Cao, X. Xia, Y. Liu, N. Wang, J. Zhang, D. Zhao, Y. Xia, *J. Power Sources* **2020**, *461*, 228130.
- [20] K. S. Hariharan, P. Tagade, S. Ramachandran, S. Springer, **2018**.
- [21] M. Doyle, J. Newman, A. S. Gozdz, C. N. Schmutz, J. Tarascon, *Electrochem. Soc. Interface* **1996**, *143*, 1890–1903.
- [22] V. Senthil Kumar, *J. Power Sources* **2013**, *222*, 426–441.
- [23] P. Gambhire, N. Ganesan, S. Basu, K. S. Hariharan, S. M. Kolake, T. Song, D. Oh, T. Yeo, S. Doo, *J. Power Sources* **2015**, *290*, 87–101.
- [24] S. Bharathraj, A. Kaushik, S. P. Adiga, S. M. Kolake, T. Song, Y. J. Sung, *Power Sources* **2021**, *494*, 229723.

Manuscript received: March 25, 2024
Revised manuscript received: April 25, 2024
Accepted manuscript online: May 13, 2024
Version of record online: June 14, 2024